FULL PAPER

ADVANCED
INTELLIGENT
SYSTEMS
Open Access

www.advintellsyst.com

Achieving Microstructure-Controlled Synaptic Plasticity and Long-Term Retention in Ion-Gel-Gated Organic Synaptic Transistors

Gyeong-Tak Go, Yeongjun Lee, Dae-Gyo Seo, Mingyuan Pei, Wanhee Lee, Hoichang Yang,* and Tae-Woo Lee*

Organic synaptic transistors using intrinsic (i.e., non-doped) organic semiconductors have demonstrated various synaptic functions to mimic biological synapses, but the devices show limited long-term retention behaviors although long-term memory is essential for neuromorphic computing. To achieve long-term retention time, correlating the synaptic responses with the microstructures of polymer semiconductor is an imperative step. It is shown that synaptic plasticity in ion-gel-gated organic synaptic transistors (IGOSTs) can be modulated by controlling the microstructure of organic semiconductors and that long-term memory retention can be significantly prolonged by increasing their crystallinity. The crystallinity of poly(3-hexylthiophene-2,5-diyl) (P3HT) films that are spun-cast on bare and self-assembled monolayer is systematically controlled, before and after thermal treatments. Long-term retention tends to extend, as the crystallinity increases. To evaluate synaptic current decay behaviors, it is suggested that the relaxation is a result of de-doping of the polymer semiconductor over time. The recognition of handwritten digits is simulated and a high classification accuracy (>92%) is achieved with IGOSTs including high crystalline P3HT film. The study provides fundamental information about the effects of polymer microstructure on synaptic plasticity of IGOSTs, which may be applicable in neuromorphic electronics.

1. Introduction

Organic synaptic transistors that mimic biological nervous system are potentially applicable to neuromorphic electronics and artificial nerve systems.[1–4] Neuromorphic electronics can overcome the limitation of von Neumann architecture, and

sensorimotor nervetronics can offer novel functions, such as perception and reflexes to sensors and robotic systems beyond the conventional electronic system.[1–3,5–7] For neuromorphic electronics, artificial synaptic devices with a two-terminal[8–11] or three-terminal structure[12–14] have emerged to mimic the synaptic functions, including short-term plasticity and long-term plasticity. Nonetheless, most organic synaptic devices are capable of only limited emulation of synaptic plasticity, either short-term or long-term, depending on whether the operation mechanism exploits either electrical double layer (EDL) formation or electrochemical redox reaction.[15–17]

Recently developed ion-gel-gated organic synaptic transistors (IGOSTs) that use a non-doped intrinsic organic semiconductor[1–3,5,13,18] have shown typical short-term plasticity behavior including short-term memory that is essential for achieving temporally correlated neuromorphic computing.[19–22] However, they usually show limited duration of long-term retention, because ions drift easily from the semiconductor to the equilibrium position after the device is turned off; this response is undesirable for computing system, because data-centric neuromorphic computing requires non-volatile long-term memory.[15,23–27]

To achieve long-term retention time, the correlation between synaptic response and microstructure in IGOSTs must be

G.-T. Go, Dr. Y. Lee, D.-G. Seo, W. Lee, Prof. T.-W. Lee
Department of Materials Science and Engineering
Seoul National University (SNU)
Seoul 08826, Republic of Korea
E-mail: twlees@snu.ac.kr

M. Pei, Prof. H. Yang
Department of Chemical Engineering
Inha University
Incheon 22212, Republic of Korea
E-mail: hcyang@inha.ac.kr

Prof. T.-W. Lee
Institute of Engineering Research
Research Institute of Advanced Materials
Nano Systems Institute (NSI)
Seoul National University (SNU)
Seoul 08826, Republic of Korea

Prof. T.-W. Lee
School of Chemical and Biological Engineering
Seoul National University (SNU)
Seoul 08826, Republic of Korea

**ADVANCED
SCIENCE NEWS**
www.advancedsciencenews.com

**ADVANCED
INTELLIGENT
SYSTEMS**
Open Access
www.advintellsyst.com

understood. This understanding requires systematic study of highly crystalline conjugated polymers of which crystallinity and microstructure can be easily tuned, unlike amorphous-like or low-crystalline isoindigo-type polymers[28] that have been used in previous polymer synaptic transistors and that have only short retention time.[19]

Here, we show that short-term and long-term synaptic plasticity in IGOSTs can be modulated by controlling the microstructure of well-ordered polymer semiconductors and demonstrate that long-term retention in IGOSTs can be significantly prolonged by controlling their microstructure. We controlled the microstructure of poly(3-hexylthiophene-2,5-diyl) (P3HT) in films spun-cast on bare substrates and on substrates that had been coated with a self-assembled monolayer (SAM), before and after thermal treatments to reveal how microstructure affects ion migration and the resulting synaptic responses. We find that long-term retention in the synaptic transistors tends to be extended, as the crystallinity of the semiconductor increases, as determined by grazing-incidence X-ray diffraction (GIXD) and optical analyses. We also suggest a triple-exponential model synaptic current decay to represent the different rates of three de-doping mechanisms of the polymer semiconductor. We simulated recognition of handwritten digits and achieved high classification accuracy (>92%) using non-volatile multi-bit IGOSTs including a highly crystalline P3HT film. Our study provides fundamental information about the effects of polymer microstructure on synaptic plasticity of IGOSTs, which can be applicable in neuromorphic electronics.

2. Results and Discussion

We fabricated "top-gate, top-contact" IGOSTs that use semiconducting P3HT films and ion-gel dielectric, which is composed of an ionic liquid and a triblock copolymer. The ionic liquid is 1-ethyl-3-methylimidazolium bis(trifluoromethylsulfonyl)imide

([EMIM][TFSI]), and the triblock polymer is poly(styrene-*b*-methyl methacrylate-*b*-styrene) (PS-PMMA-PS). To fabricate IGOSTs, P3HT was spun-cast on bare Si/SiO_2 substrates or Si/SiO_2 substrates that had been treated with octadecyltrimethoxysilane (ODTS) to form an SAM. The spin-cast solution was composed of 3 mg of P3HT in 1 mL of chlorobenzene.

To achieve long-term retention in IGOSTs, we further modulated the microstructure of the P3HT by thermally annealing some films at 150 °C for 10 min. Therefore, four P3HT films were obtained: 1) as-spun@bare (as-spun on bare Si/SiO_2 substrate); 2) annealed@bare (annealed on bare Si/SiO_2 substrate); 3) as-spun@SAM (as-spun on SAM-treated substrate); and 4) annealed@SAM (annealed on SAM-treated substrate). The crystallinity was highest in an annealed@SAM P3HT, while lowest in as-spun@bare film; this result is consistent with the previous reports.[29,30]

IGOSTs can emulate the signaling mechanism of biological synapses and demonstrate synaptic characteristics that are similar to the various functionalities of the brain, such as short-term and long-term changes.[31] In the devices, presynaptic gate-voltage spikes V_G applied to the gate electrode trigger a post-synaptic current (PSC) at the drain electrode; the amplitude of the PSC can be modulated by migration of ions from an ion-gel gate dielectric to a semiconducting polymer layer; this process is similar to the way that presynaptic action potentials trigger postsynaptic signals by releasing neurotransmitters from a preneuron to postsynaptic membrane through a synaptic cleft (**Figure 1**). For the IGOSTs used in this study, we applied a presynaptic voltage spike $V_G = -1.5$ V, which is large enough to inject ions into both the amorphous and crystalline parts of P3HT film.[32–34] Subsequent back diffusion of ions from the amorphous or crystalline regions reduces the conductance of the semiconducting polymer films, so PSC decays at the drain electrode of the IGOST.

In general, a large clockwise hysteresis of drain current–gate voltage (I_D–V_G) transfer curves of IGOSTs indicates migration and despreading of ions in polymer bulk film of IGOSTs[35]
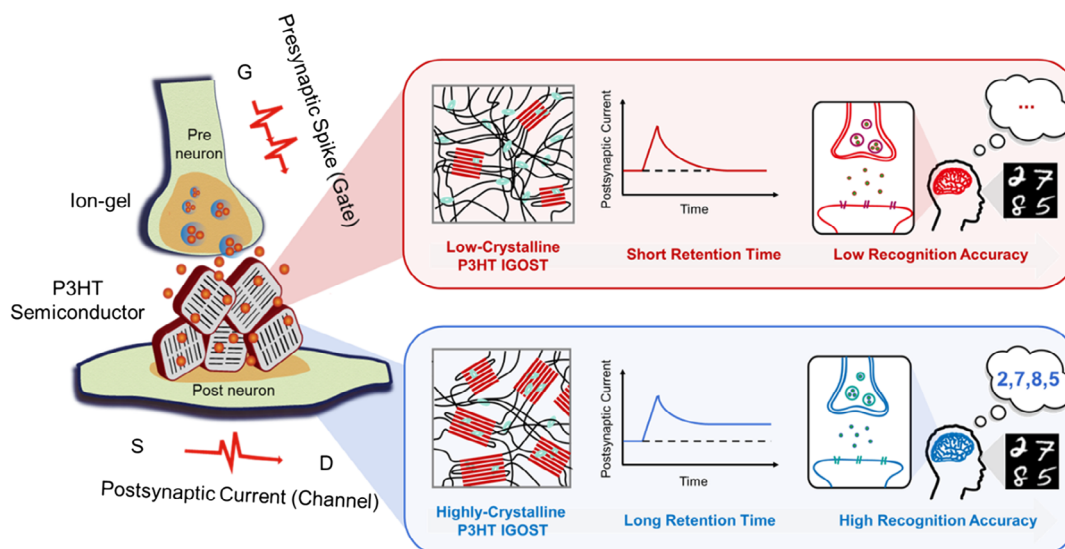

Figure 1. Schematic illustration of IGOST (left) and microstructure-controlled synaptic plasticity (right) in low-crystalline P3HT IGOST (right, top) and highly crystalline P3HT IGOST (right, bottom). Change of microstructure leads to change of long-term synaptic plasticity, which affects recognition accuracy for neuromorphic computing.

(Figure S1, Supporting Information); this mechanism suggests that synaptic behaviors can be controlled by ion motions in the polymer semiconductors.

An as-spun P3HT film on the bare SiO_2 surface contained the largest portion of amorphous regions. After 50 presynaptic spikes, most of amorphous regions in the low crystalline P3HT (as-spun@bare) film would be filled by the anions, which can be easily diffused into a P3HT film even at low driving voltage (Figure 1, upper).[32] After turning off the voltage spikes, these anions also easily diffuse out of the low-crystalline P3HT film, especially in amorphous regions,[34,36] so PSC rapidly decayed; this response is analogous to short-term retention in biological synapses (**Figure 2**a). In contrast, in the high crystalline P3HT (annealed@SAM) film, the portion of crystalline regions would be the highest, and grain size would be the largest (Figure 1, bottom).[29] π-conjugated backbone planes with a strong intermolecular $\pi-\pi$ interaction are much more resistant than side-chain allocated regions against diffusion of anions. Anions that enter interdigitated regions are surrounded by $\pi-\pi$ overlapped backbones of P3HT. So, the anions may be trapped for a long time, in comparison with anions in the amorphous area (Figure 2b).[32,33] The ion trapping could lead to stable current retention in long-term potentiation, which is important for implementing long-term memory behavior in neuromorphic computing.[11,37] In an IGOST with an ODTS annealed film, PSC was retained after 12 min without any noticeable decay; the current retention was clearly different from that of the as-spun@bare film, in which PSC decays within a few minutes.

During the continuous current reading, PSC in the IGOST that used annealed@SAM film started to increase slightly after 10 min; this change may be caused by moisture absorption by the ion gel in ambient air.[38,39] However, all devices were measured in the same ambient condition, and the as-spun@bare IGOST showed fast decay, and moisture did not significantly affect the trend in device characteristics. Thus, we achieved long and stable long-term retention based on spike number-dependent plasticity (SNDP) in IGOSTs by controlling the microstructure of P3HT.

To obtain non-volatile and stable memory states for neuromorphic computing, long-term memory retention by organic artificial synapses is essential. As the number of spikes was increased from 5 to 50, PSC converged to different levels that correspond to different memory states (Figure 2c, and Figure S2, Supporting Information). Especially, IGOST with the ODTS annealed film, which had the highest crystallinity, showed more fluent current decay and more stable current retention than other devices (Figure 2c, and Figure S2, Supporting Information).

Memory states were reversibly controlled by synaptic potentiation and depression. By applying negative spikes (-2 V, 80 ms, five spikes) and positive spikes (1 V, 80 ms, four spikes), two memory states were reliably controlled in the IGOST that used an ODTS annealed P3HT film (Figure 2d). The non-volatile multi-bit memory states driven by these spikes may help to achieve neuromorphic computing. The following results highlight that our IGOSTs have advantages in emulating various synaptic plasticity including both short-term plasticity and long-term
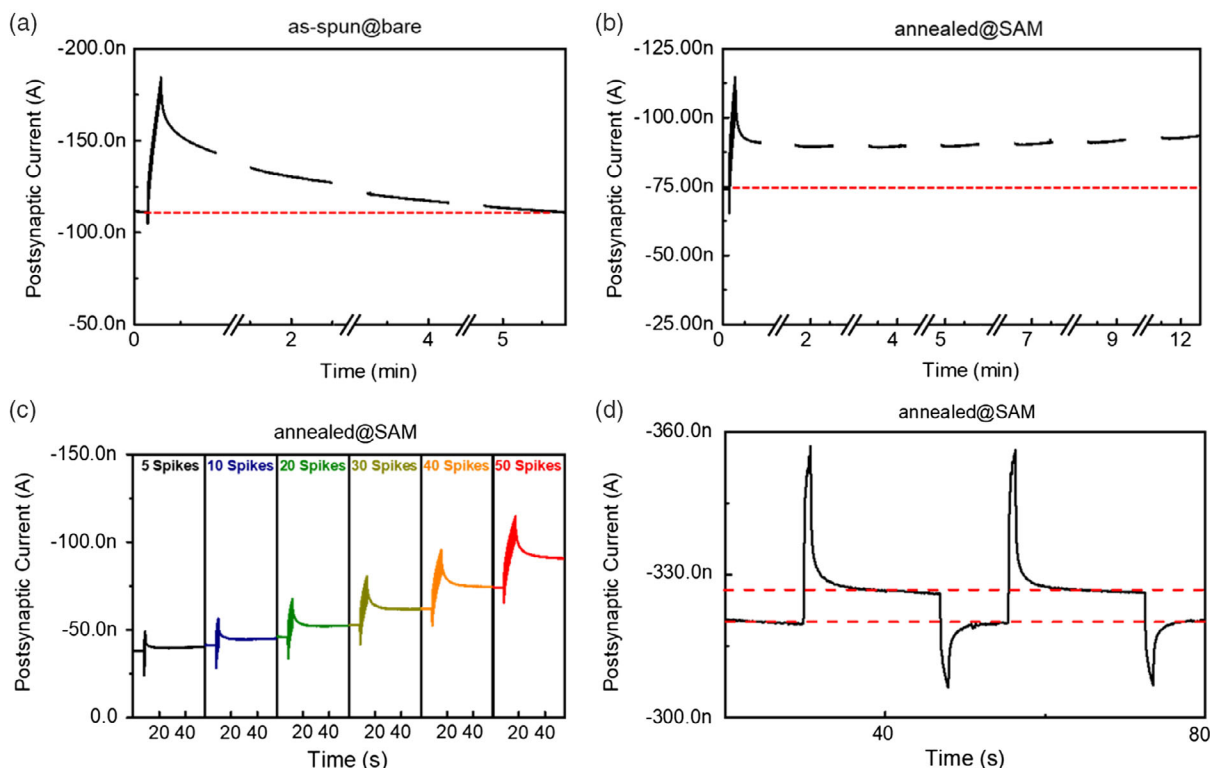

Figure 2. Synaptic properties of IGOSTs. Memory retention of a) as-spun@bare IGOST and b) annealed@SAM IGOST by applying gate spikes ($V_G = -1.5$ V, 80 ms) with a V_D of -0.45 V as reading voltage. Red dotted line: initial current. c) SNDP with 5–50 spikes and d) controlled memory states by five subsequent potentiation spikes (-2 V, 80 ms) and four depression spikes (1.5 V, 80 ms) in annealed@SAM IGOST.

plasticity with low energy consumption that is desired for neuro-inspired electronics (Table S1, Supporting Information).

Paired-pulse facilitation (PPF) is an important synaptic characteristic of short-term potentiation. PPF is initiated by two consecutive stimuli with short interval Δt between them. Because of the short Δt, ion migration increases, so the second PSC is stronger than the first PSC. The intensity ratio, PPF index (A_2/A_1), between the heights of the first PSC peak A_1 and the second PSC peak A_2, represents the effect of Δt on relationship in PPF (Figure S3, Supporting Information).[3,11,13,40]

Spike frequency-dependent plasticity (SFDP) also represents short-term plasticity, which is a possible method of unsupervised learning.[41] SFDP was obtained by applying five consecutive spikes at frequencies $3.8 \leq f_S \leq 8\,Hz$ (Figure S3, Supporting Information). The SFDP index A_5/A_1 increased with increasing f_S (Figure S3, Supporting Information).

UV–Vis absorption of the P3HT films was measured to quantify their crystalline quality (**Figure 3**a). The absorbance peak at a wavelength of $\lambda_P \approx 550\,nm$ corresponds to the 0–1 vibrational transition of neutral P3HT (Figure 3b).[42,43] Amorphous chains have a more disordered structure that has lower conjugation length and more conformation defects than the crystalline parts. Therefore, amorphous chains absorb higher energy than crystalline parts, and this effect leads to a redshift in λ_P.[42,44–46] Thermal annealing and SAM treatment caused the redshift in λ_P; this change suggests that the annealing caused increases in the concentrations of aggregates and crystallites (**Table 1**).[47,48] The intensity ratio of 0–0 to 0–1 vibrational transitions is greater

Table 1. Summary of the structure information in UV–Vis absorption of the P3HT film.

P3HT film	UV–Vis absorption peak wavelength [nm]	Excitonic bandwidth W [meV]
as-spun@bare	541	160
annealed@bare	546	141
as-spun@SAM	549	128
annealed@SAM	553	127

in crystalline regions than in amorphous regions;[49] the difference represents the degree of excitonic coupling in crystallites.[50] Crystalline quality can be evaluated by measuring excitonic bandwidth (W, Equation (1)).[48]

$$\frac{A_{0-0}}{A_{0-1}} = \left[\frac{1 - \left(\frac{0.24W}{E_P}\right)}{1 + \left(\frac{0.073W}{E_P}\right)} \right]^2 \tag{1}$$

where A_{0-n} ($n \in \{0, 1\}$) is the intensity of the 0–n transition, and $E_P = 0.18\,eV$ is the energy of the main intermolecular vibration. W decreases with an increase in intra-chain ordering and conjugation length of P3HT chains.[48] W was obtained, assuming a Huang–Rhys factor of 1.[48,51] W decreased after thermal annealing and SAM treatment; these changes coincided with the
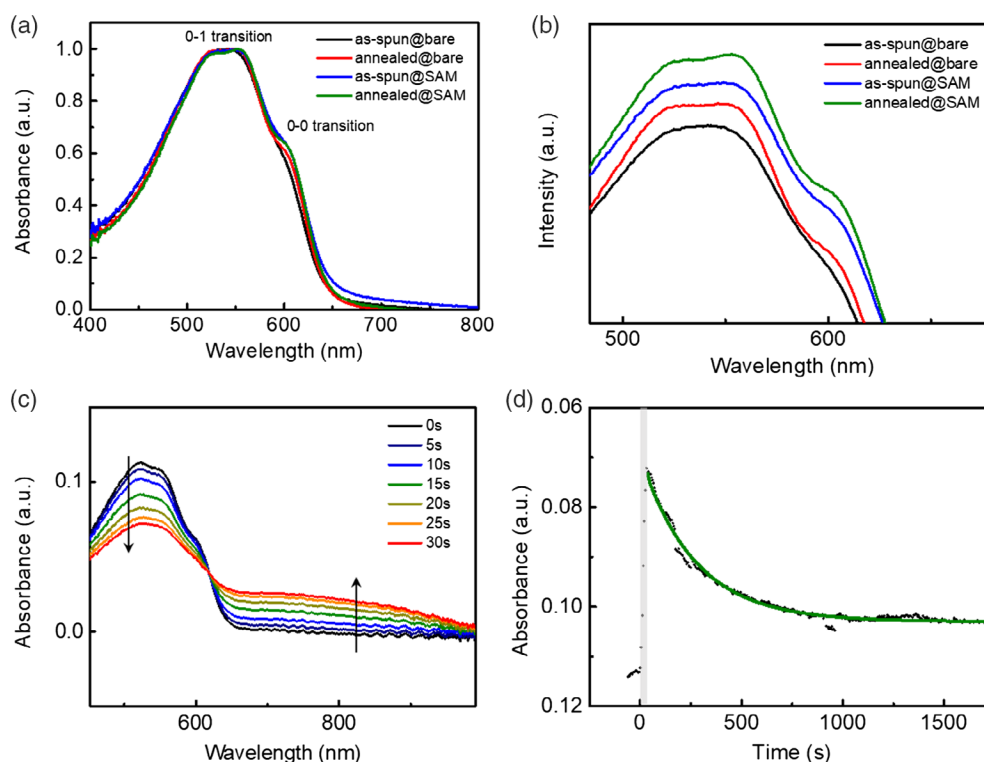

Figure 3. UV–Vis absorption spectra of the P3HT films. a) UV–Vis absorption spectra of the P3HT film. b) Enlarged absorption spectra of the P3HT films at a wavelength of $\approx 550\,nm$. c) Spectral changes in UV–Vis absorption during real-time electrochemical reaction of P3HT film. Arrow: direction of bleaching feature of neutral P3HT as polaron formation. d) Spectral changes in the UV–Vis absorption during spontaneous de-doping of P3HT film over time after doping process in (c). Black dots: Measured absorbance value of P3HT film every 5 s. Green line: Fitted line.

redshift of λ_P. A decrease in W and redshifts in λ_P indicate that the crystallinity of P3HT film increased after thermal annealing and SAM treatment.

Real-time UV–Vis absorbance was also measured for P3HT films to characterize the ion doping-driven electrochemical reaction, which is the main operational mechanism of IGOSTs.[52] UV–Vis absorption spectra were measured for P3HT film on indium tin oxide (ITO)/polyethylene terephthalate substrate placed in ion-gel solution (Figure S5, Supporting Information). Constant voltage (-1.5 V, 30 s) was applied to the ion gel, and ITO was grounded to induce electrochemical reaction of P3HT film by doping with anions. While voltage was applied, the intensity of the peak of neutral P3HT at a wavelength of $\lambda \approx 550$ nm decreased, and the peak of oxidized P3HT at

$\lambda \approx 800$ nm increased (Figure 3c).[53] TFSI anions induce oxidized doping of P3HT with polaron formation. In addition, the peak of the 0–0 transition initially decreased relative to the peak of the 0–1 transition. Crystallites show high A_{0-0}/A_{0-1},[33] so we confirm that crystalline region and amorphous region were both oxidized, but more in crystalline regions than in amorphous regions. After the voltage was turned off, the decrease in the spectral peak at $\lambda \approx 550$ nm slowly recovered, but did not reach its original intensity (Figure 3d). This response indicates that some of the anions that penetrated the P3HT film might have remained in it for a long time. This result may contribute to the origin of current-retention behavior in long-term plasticity.

The 2D GIXD patterns (Figure 4a) were obtained from all of the P3HT films. All of the P3HT films contained edge-on and
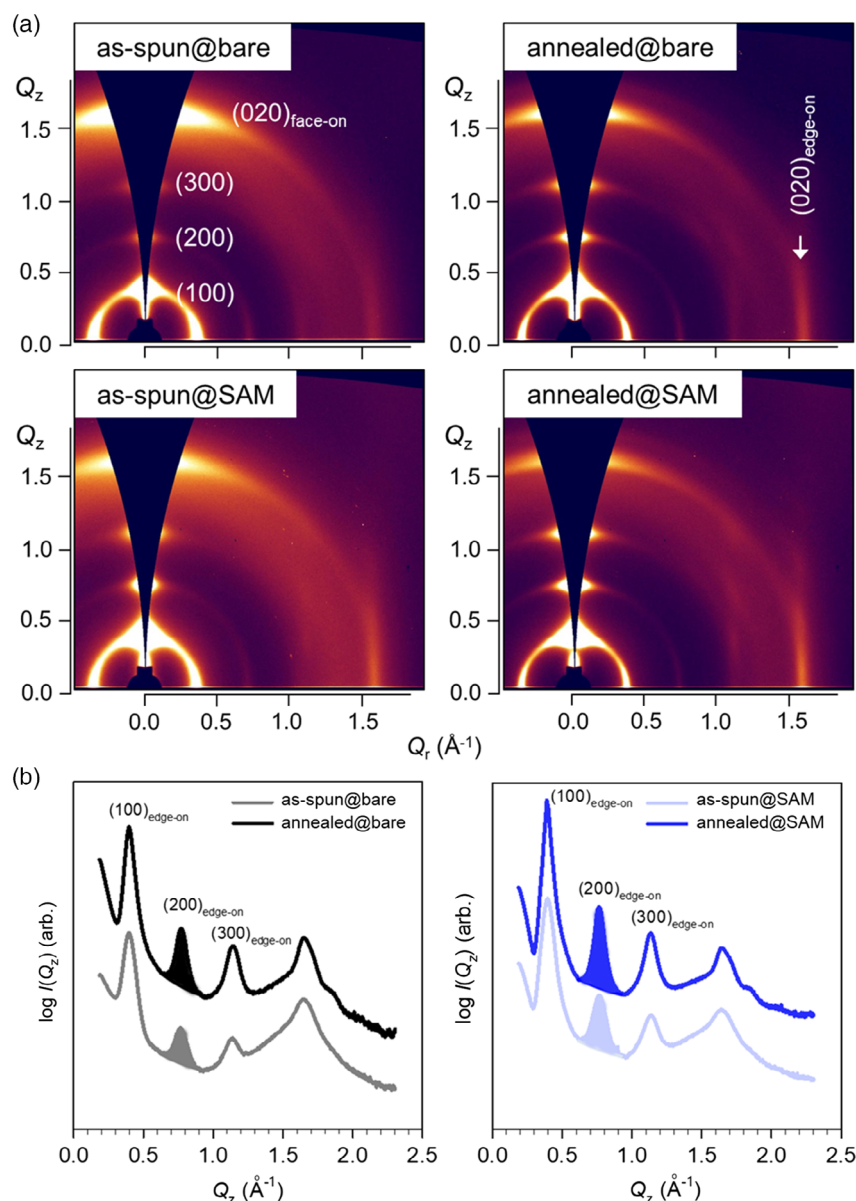

Figure 4. a) 2D GIXD patterns of the as-spun and annealed P3HT films on bare and ODTS-treated SiO$_2$ surfaces. b) 1D out-of-plane X-ray profiles extracted along the Q_z axis from (a).

face-on preferred orientations of P3HT chains on the surfaces, as determined by clear (020) reflections along both the Q_z and Q_r axes in the GIXD patterns.[54] After annealing at 150 °C for 10 min, both the crystallinity and edge-on orientation of the semiconducting polymer chains were considerably increased, as determined by intense (h00) reflections along the Q_z axis. The 1D out-of-plane X-ray profiles extracted along the Q_z axis (Figure 4b) indicate that of the film crystallinity decreased in the order: annealed@SAM >> annealed@bare > as-spun@SAM > as-spun@bare. Average domain sizes D_c (referred as coherence length) in the P3HT films were calculated (**Table 2**) from (200) crystal reflections (color-filled areas in Figure 4b) and the

Scherrer equation $D_C = K\lambda/(\beta\cos\theta)$, where $K = 0.9$ is a dimensionless shape factor, $\lambda = 1.0688$ Å is the X-ray wavelength, θ is the Bragg angle at (200) reflection, and β is the full width at half maximum (FWHM). The annealed@SAM film had $D_C = 19.3$ nm, whereas the as-spun@bare film had $D_C = 13.6$ nm.

Atomic force microscopy (AFM) was used to obtain the topographies (**Figure 5**) of all four films. All had smooth surfaces with low root-mean-square roughness $0.64 \leq R_q \leq 0.87$ nm, so it was not much affected by the coating surface or annealing. The solvent evaporates rapidly during spin-casting, so the high-M_w P3HT chains could grow only to granular nanodomains, rather than to nanofibrils.[30,55] The crystallinity and domain size of P3HT were clearly distinguished in these films. The as-spun@bare film showed weakly ordered structure, whereas the annealed@SAM film contained densely compacted, granular nanodomains. The AFM results indicated that the average domain diameter D_{AFM} in the P3HT films increased, as the crystallinity of films increased (Table 2). The as-spun@bare film had the lowest $D_{AFM} = 25.8$ (± 3.80) nm, and ODTS annealed films had the highest $D_{AFM} = 37.5$ (± 7.0) nm. The trend of the variation in D_{AFM} matched that of D_C, although the domain sizes differed slightly because of the different measurement methods.[56] Therefore, the GIXD and AFM results demonstrate that SiO_2 surface treatment and additional annealing changed the crystalline structures of P3HT in the spun-cast films from weakly ordered to highly crystalline granular texture. P3HT films that exhibited long-term memory retention had high crystallinity, large domain size, and small domain-boundary density.
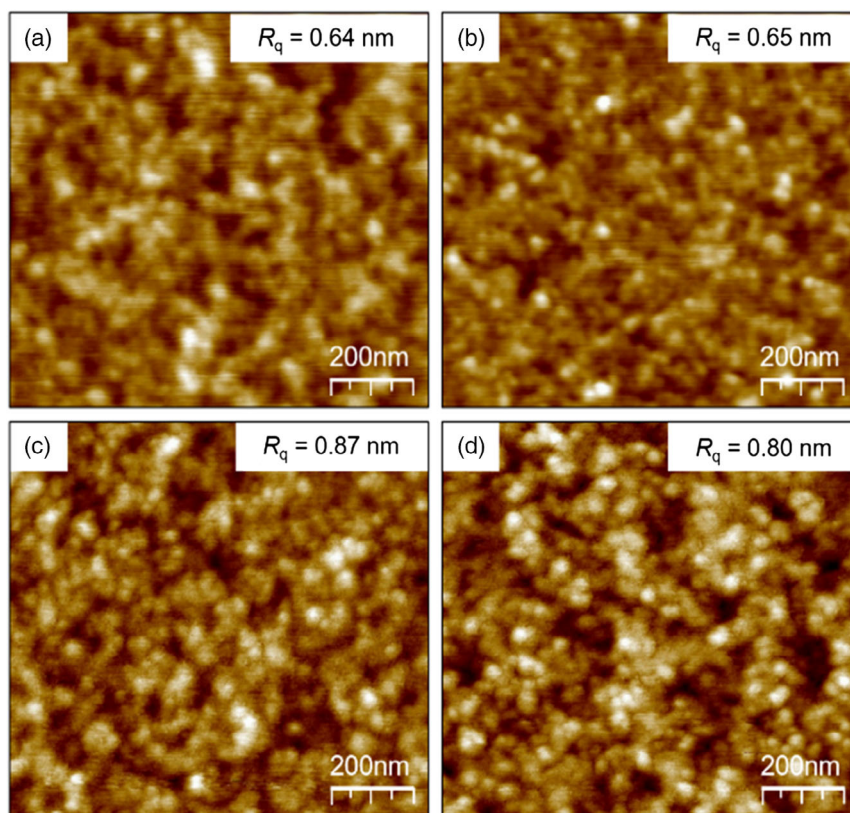
Table 2. Summary of the structural information in GIXD profile of the P3HT film.

P3HT film	$\Delta Q_{(h00)}$ [Å^{-1}][a]	$d_{(h00)}$ [Å]	$Q_{(010)}$ [Å^{-1}][b]	$d_{(010)}$ [Å]	FWHM $Q_{(200)}$ [Å^{-1}][c]	D_c [nm][d]	D_{AFM} [nm][e]
as-spun@bare	0.378	16.62	1.64	3.831	0.0836	13.558	25.3 ± 3.8
annealed@bare	0.377	16.67	1.64	3.831	0.0733	15.467	25.8 ± 3.0
as-spun@SAM	0.372	16.89	1.64	3.822	0.0733	15.467	31.2 ± 11.5
annealed@SAM	0.375	16.76	1.64	3.827	0.0586	19.332	37.5 ± 7.0

[a] Extracted along the Q_z axis; [b] Extracted along the Q_r axis; [c] Determined from (200)$_{edge-on}$ reflections; [d] Coherence length $D_c = K\lambda/(\beta\cos\theta)$; $K = 0.9$; $\lambda = 1.0688$ Å; $\theta = \arcsin(q\lambda/4\pi)$; [e] Calculated from AFM topographies; ± standard deviation.

Figure 5. AFM topographies of P3HT films: a) as-spun@bare, b) annealed@bare, c) as-spun@SAM, and d) annealed@SAM P3HT films.

To evaluate long-term current retention characteristics of IGOSTs, we propose a model that divides PSC decay into three regimes that consider the microstructure of the P3HT. This model has one more regime than the previously reported-current decay curve in IGOSTs.[52] The PSCs were fitted using a tri-exponential function to describe the PSC decay I after 50 spikes as

$$I = I_1 \exp(-t/\tau_1) + I_2 \exp(-t/\tau_2) + I_3 \exp(-t/\tau_3) + I_0$$
$$(\tau_1 < \tau_2 < \tau_3) \tag{2}$$

where I_0 is the resting current before application of spikes, I_1, I_2, and I_3 are the pre-factors of PSC, and τ_1, τ_2, and τ_3 are their time constants. This equation divides the decay response of the current into three parts, because IGOST has three major dynamics: 1) depolarization of EDLs (τ_1); 2) anion de-doping from amorphous regions (τ_2); and 3) anion de-doping from crystalline regions (τ_3) of P3HT film. This decay curve model agrees well

with the measured PSC results ($R^2 \approx 0.999$) (**Figure 6**a,b, and Figure S6, Supporting Information). Our proposed mechanism (Figure 6c) suggests that each time constant has a different scale: $\tau_1 < 1$ s and $\tau_2 < 7$ s are relatively short, but $\tau_3 > 100$ s is relatively long. Depolarization of EDLs is a fast process that takes in <1 s;[52,57] therefore, we can hypothesize that the exponential decay with time constant τ_1 is a result of depolarization.

We confirmed by optical analysis that both amorphous and crystalline regions were doped. Amorphous and crystalline regions have different de-doping kinetics. Ion diffusion into the amorphous regions requires relatively low voltage,[32,33] so spontaneous diffusion out of the polymer bulk would be easy. In contrast, penetration of ions into interdigitated alkyl side chains in the crystalline region requires high driving voltage.[32,33] These ions become tightly bound[32] in the crystallites and, therefore, cannot easily diffuse out of the polymer bulk. This difference in ease of ion migration from amorphous regions and crystalline regions leads to two different regimes
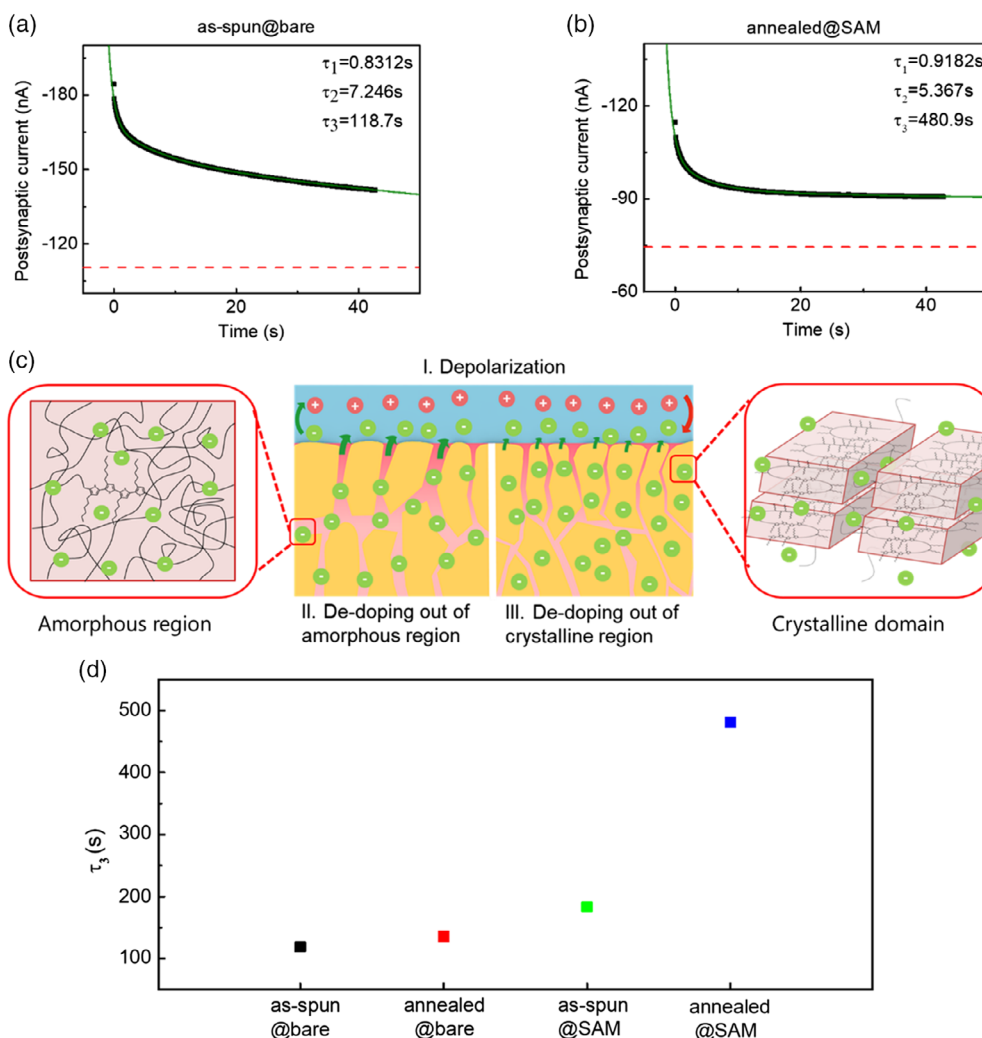

Figure 6. Long-term current decay model of IGOSTs. Fitting with tri-exponential model of a) as-spun@bare IGOST and b) annealed@SAM IGOST. Red lines: initial current before potentiation; blue lines: PSC values fitted by tri-exponential decay model; black squares: measured PSCs. c) Hypothesized mechanism of tri-exponential decay curve. Each time constant has a suggested physical meaning: 1) depolarization (τ_1), 2) de-doping from the amorphous region (τ_2), and 3) de-doping from the crystalline region (τ_3). d) τ_3 in tri-exponential decay curves of IGOSTs.
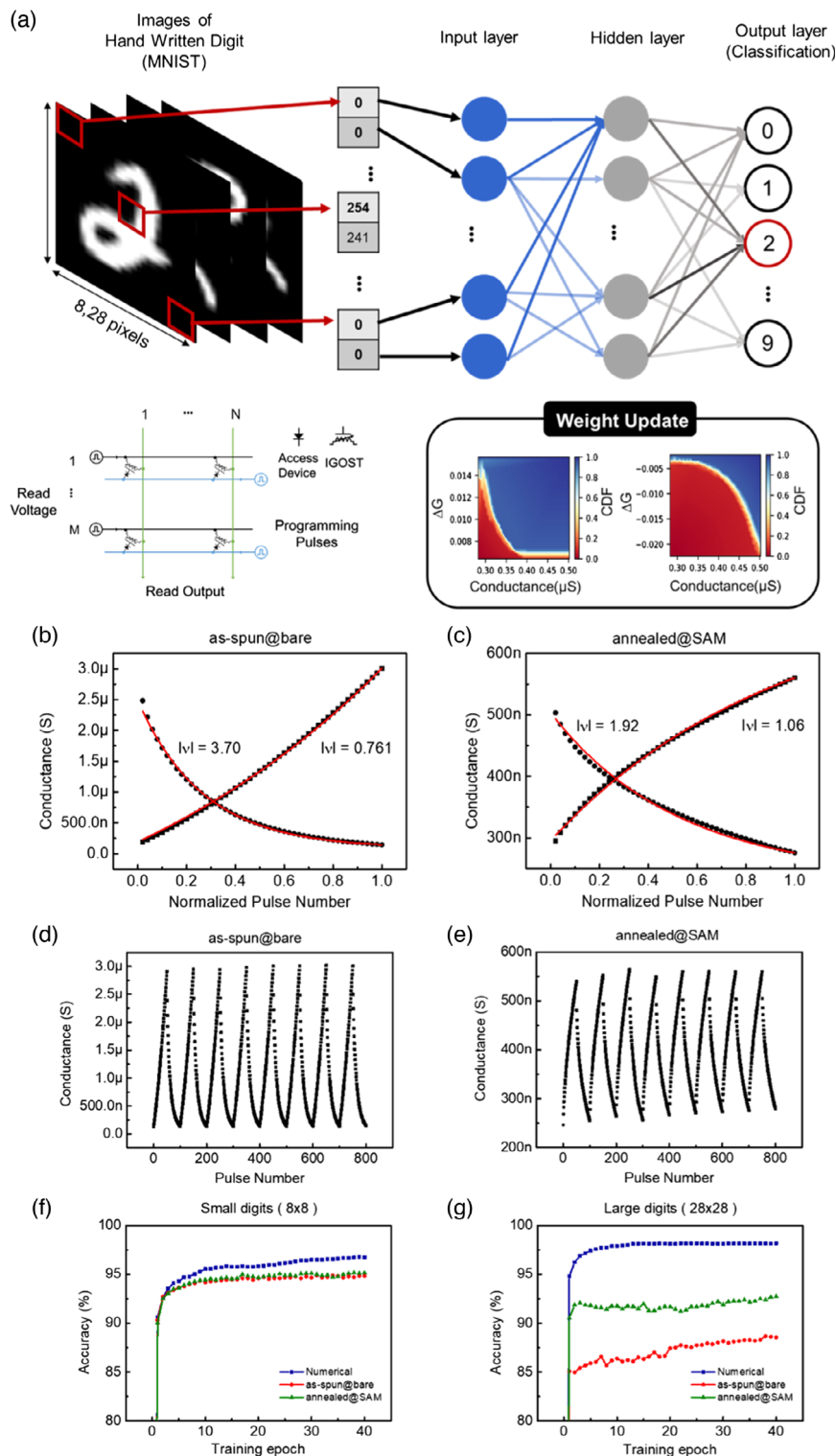
Figure 7. Multi-conductance states and simulation of hand-written digit recognition of IGOSTs. a) Schematics of neural network (top) and IGOST cross bar array (bottom, left) for a simulation of recognition of hand-written digits. All synaptic weights are uploaded by conductance of the device (bottom, right); CDF is cumulative distribution function. Conductance states of b) as-spun@bare IGOST and c) annealed@SAM IGOST with 50 potentiation (−1.5 V, 220 ms) and 50 depression (1.5 V, 220 ms) pulses. Linearity parameter ν is calculated by conductance fitting (red line). Eight repeated cycles of potentiation and depression curves in d) as-spun@bare IGOST and e) annealed@SAM IGOST. Simulation of hand-written digit recognition by Cross-Sim. Training accuracy of f) small digits (8 × 8) and g) large digits (28 × 28, MNIST) data recognition; training accuracy of ideal numerical device, as-spun@bare IGOST, and annealed@SAM IGOST.

**ADVANCED
SCIENCE NEWS**

www.advancedsciencenews.com

**ADVANCED
INTELLIGENT
SYSTEMS**
Open Access

www.advintellsyst.com

of de-doping. Therefore, we suggest that the time constant τ_2 corresponds to anion de-doping from the amorphous regions in the polymer bulk and that τ_3 corresponds to anion de-doping from the crystalline regions in the polymer bulk.

In this model, τ_3 represents long-term retention characteristics. Depending on the microstructures, τ_3 was remarkably increased in the annealed@SAM IGOST ($\approx$480 s) (Figure 6d). This increase occurs, because the P3HT had increased crystallinity and crystal domain size; both of these traits may greatly suppress back diffusion of anions that penetrated crystallites. This hypothesis suggests that long-term current retention can be controlled by crystallinity of the polymer films. Although other factors can affect PSC decay behaviors of synaptic transistors, we believe that the polymer microstructure has a strong effect on synaptic plasticity.

Non-volatile multi-bit memory for neuromorphic computing requires various conductance states. We simulated recognition by an artificial neural network (ANN) that is composed of an IGOST crossbar array (**Figure 7**a). The conductance G_I, which is the synaptic weight in ANN, is updated by a back-propagation mechanism. Distinct multiple G_I states of the IGOSTs were modulated by applying series of 50 potentiation spikes (-1.5 V, 220 ms) and 50 depression spikes (1.5 V, 220 ms) (Figure 7b,c). G_I was measured at saturation time, which is defined as the time t when conductance exhibits deviations $\Delta G_I(t) = 1 - |I_t/I_{t-0.05}| < 0.5\%$, where $\Delta G_I(t)$ is the variation at time t, I_t is the current at t, and $I_{t-0.05}$ is the current of the previous measurement point, with 0.05 s as the time between successive measurements. The linearity of potentiation and depression curves is a sign of uniform conductance change, which is important for high accuracy of pattern recognition by ANNs.[58] To define the linearity of the curve, G was fitted using Equation (3) for potentiation and Equation (4) for depression.[59,60]

$$G = G_1(1 - e^{-\nu P}) + G_{min}, \quad G_1 = \frac{G_{max} - G_{min}}{1 - e^{-\nu}} \quad (3)$$

$$G = G_2(1 - e^{-\nu P}) + G_{max}, \quad G_2 = -\frac{G_{max} - G_{min}}{1 - e^{-\nu}} \quad (4)$$

where P is the pulse number normalized by 50 total pulses, ν is the linearity of curve (ν close to 0 means linear), G_{max} is the maximum conductance, and G_{min} is the minimum conductance.

Both IGOSTs showed higher linearity in potentiation curves than in depression curves; the difference may be a result of the different kinetics of ion migration between voltage-induced penetration and back diffusion in the P3HT bulk. The devices had potentiation curves with similar ν (0.76 for as-spun@bare and 1.06 for annealed@SAM), but depression curves with quite different ν (3.70 for as-spun@bare and 1.92 for annealed@SAM); i.e., the linearity increased, as crystallinity of P3HT increased. This improved linearity during depression might be caused by suppression of rapid back diffusion of ions during early stages of depression. With repeated application of potentiation and depression pulses, both IGOSTs showed reproducible changes in G and low cycle-to-cycle variation (Figure 7d,e). This simulation has ignored other factors, such as decay of current over time and device-to-device variation, which affects the yield of array fabrication. Nonetheless, we expect that improved retention duration would reduce the change in conductance over time.

To demonstrate ANN by our IGOSTs, recognition of handwritten digits was simulated for a three-layer ANN (input layer, hidden layer, and output layer). The ANN was trained using the MNIST datasets, which consist of 8 × 8 pixel and 28 × 28 pixel images of handwritten digits.[5,61–63] Analysis of small digits (8 × 8 pixel) using an ANN composed of IGOSTs with as-spun@bare film or annealed@SAM film both obtained high training accuracy, which was very close to numerical training results (Figure 7f). In contrast, analysis of large digits (28 × 28 pixel) obtained slightly lower training accuracy (86.8% for the IGOST with as-spun@bare film and 92.7% for the device with annealed@SAM film) than the numerical value of 98.2% (Figure 7g). The increase in the accuracy by the ANN that used IGOST with the annealed@SAM (high-crystallinity) film compared with the device with the as-spun@bare (low-crystallinity) film may be a result of the higher linearity of the depression curve in the annealed@SAM than in the as-spun@bare film.[64] These results prove that our strategy to develop IGOSTs can make them viable candidates for use in neuromorphic computing.

3. Conclusion

We fabricated IGOSTs with long-term memory retention. They were composed of a microstructure-controlled intrinsic semiconducting polymer film and an ion-gel gate dielectric layer. IGOSTs emulate various synaptic properties, such as PPF, SFDP, SNDP, and long-term plasticity. Especially, the retention time of long-term plasticity was remarkably prolonged in IGOSTs, as the crystallinity of the semiconducting polymer film was increased, because the increased crystallinity can suppress rapid back diffusion of ions that penetrated the semiconducting polymer film. The crystallinity of semiconducting polymer was proved using GIXD and optical analysis. To represent the long-term plasticity of IGOSTs, a tri-exponential model of PSC decay is proposed to explain the de-doping nature of semicrystalline polymer; the exponentials represent 1) rapid EDL depolarization; 2) relatively fast ion diffusion out of amorphous regions; and 3) slow ion diffusion out of crystalline regions. In recognition of handwritten digits by ANNs that use our IGOSTs, ANNs that used IGOSTs based on highly crystalline semiconducting polymer achieved high classification accuracy. This high accuracy suggests that IGOSTs have applications in future brain-inspired neuromorphic computing. Our work has shown how the microstructure of polymer semiconductors in IGOSTs can affect the synaptic plasticity; the information will be useful to guide the development of neuromorphic computing, soft robotics, and neural prosthetics.

4. Experimental Section

SAM Deposition: SAM treatment was conducted as described previously.[65] ODTS solution (1 µg mL^{-1}) (ODTS, Sigma-Aldrich) in trichloroethylene (TCE; >99%, Sigma-Aldrich) was spin-coated on UV ozone-treated Si/SiO$_2$ wafers at 2000 rpm for 30 s. Then, the ODTS-cast substrates were put into a vacuum desiccator for 12 h with a vial that contains ammonium hydroxide solution ($\approx$25% in water, Sigma-Aldrich). Then, the substrates were rinsed in toluene to eliminate excess ODTS molecules.

**ADVANCED
SCIENCE NEWS**

www.advancedsciencenews.com

**ADVANCED
INTELLIGENT
SYSTEMS**
Open Access

www.advintellsyst.com

Device Fabrication: P3HT solution (3 mg mL^{-1}) (P3HT; Sigma-Aldrich) in chlorobenzene (Sigma-Aldrich) was spin-coated on bare and ODTS-treated Si/SiO$_2$ substrates at 2000 rpm for 30 s. The devices were thermally annealed at 150 °C for 10 min under N$_2$ atmosphere. Au was thermally evaporated to form source and drain electrodes (40 nm) through shadow masks in a high vacuum chamber ($\approx10^{-6}$ Torr). The defined channel was 50 µm long and 1500 µm wide.

Ion gel composed of PS-PMMA-PS triblock copolymer (Polymer Source), ionic liquid [EMIM][TFSI] (Sigma-Aldrich), and ethyl acetate (Sigma-Aldrich) (1:9:90, w:w:w) was drop-cast on the channel area; then, the devices were dried in a vacuum chamber (10^{-3} Torr) for 12 h.

Characterization: UV–Vis absorption spectra were obtained using a PerkinElmer Lambda 465 UV/Vis Spectrophotometer. The 2D GIXD was performed on the films at beamlines 6D and 9A at the Pohang Accelerator Laboratory (PAL), Republic of Korea; the incident angle of the X-ray beam ($\lambda = 1.0688$ Å) on a sample was fixed at 0.12°. AFM (Multimode 8, Bruker) was performed on the P3HT films. All electrical characteristics of the devices were measured in ambient condition using a Keysight B1500A semiconductor parameter analyzer. Potentiation and depression curves were obtained after application of five cycles with −2.8/2.8 V pulses and 20 cycles of −1.5/1.5 V pulses for stabilization.

Array Simulation: Array was simulated using "Cross Sim" (Sandia National Laboratory, USA). A three-layer (784 × 300 × 10) network was used for analysis of all datasets of MNIST images. Training used 60 000 example images and testing used 10 000 images. The learning rate was 0.1 for numerical calculations and for IGOST with annealed film and 0.05 for IGOST with as-spun@bare film.

Conflict of Interest

The authors declare no conflict of interest.

[1] Y. Lee, T.-W. Lee, *Acc. Chem. Res.* **2019**, *52*, 964.

[2] Y. Kim, A. Chortos, W. Xu, Y. Liu, J. Y. Oh, D. Son, J. Kang, A. M. Foudeh, C. Zhu, Y. Lee, S. Niu, J. Liu, R. Pfattner, Z. Bao, T.-W. Lee, *Science* **2018**, *360*, 998.

[3] Y. Lee, J. Y. Oh, W. Xu, O. Kim, T. R. Kim, J. Kang, Y. Kim, D. Son, J. B.-H. Tok, M. J. Park, Z. Bao, T.-W. Lee, *Sci. Adv.* **2018**, *4*, eaat7387.

[4] S. Jang, S. Jang, E.-H. Lee, M. Kang, G. Wang, T.-W. Kim, *ACS Appl. Mater. Interfaces* **2019**, *11*, 1071.

[5] Y. Van De Burgt, E. Lubberman, E. J. Fuller, S. T. Keene, G. C. Faria, S. Agarwal, M. J. Marinella, A. Alec Talin, A. Salleo, *Nat. Mater.* **2017**, *16*, 414.

[6] H.-L. Park, H. Kim, D. Lim, H. Zhou, Y.-H. Kim, Y. Lee, S. Park, T.-W. Lee, *Adv. Mater.* **2020**, 1906899.

[7] H.-L. Park, Y. Lee, N. Kim, D.-G. Seo, G.-T. Go, T.-W. Lee, *Adv. Mater.* **2019**, 1903558.

[8] S. H. Jo, T. Chang, I. Ebong, B. B. Bhadviya, P. Mazumder, W. Lu, *Nano Lett.* **2010**, 1297.

[9] X. Zhao, H. Xu, Z. Wang, Y. Lin, Y. Liu, *InfoMat* **2019**, 183.

[10] Y. Li, Z. Wang, R. Midya, Q. Xia, J. J. Yang, *J. Phys. D. Appl. Phys.* **2018**, *51*, 503002.

[11] W. Xu, H. Cho, Y.-H. Kim, C. Wolf, C.-G. Park, T.-W. Lee, *Adv. Mater.* **2016**, 5916.

[12] C. J. Wan, Y. H. Liu, P. Feng, W. Wang, L. Q. Zhu, Z. P. Liu, Y. Shi, Q. Wan, *Adv. Mater.* **2016**, 5878.

[13] W. Xu, S.-Y. Min, H. Hwang, T.-W. Lee, *Sci. Adv.* **2016**, *2*, 1.

[14] Y. H. Liu, L. Q. Zhu, P. Feng, Y. Shi, Q. Wan, *Adv. Mater.* **2015**, *27*, 5599.

[15] L. An Kong, J. Sun, C. Qian, Y. Fu, J. Wang, J. Yang, Y. Gao, *Org. Electron.* **2017**, *47*, 126.

[16] C. Qian, L. an Kong, J. Yang, Y. Gao, J. Sun, *Appl. Phys. Lett.* **2017**, *110*, 1.

[17] P. Gkoupidenis, N. Schaefer, B. Garlan, G. G. Malliaras, *Adv. Mater.* **2015**, *27*, 7176.

[18] Y. van de Burgt, A. Melianas, S. T. Keene, G. Malliaras, A. Salleo, *Nat. Electron.* **2018**, *1*, 386.

[19] D.-G. Seo, Y. Lee, G.-T. Go, M. Pei, S. Jung, Y. H. Jeong, W. Lee, H.-L. Park, S.-W. Kim, H. Yang, C. Yang, T.-W. Lee, *Nano Energy* **2019**, *65*, 104035.

[20] Y. He, S. Nie, R. Liu, S. Jiang, Y. Shi, Q. Wan, *Adv. Mater.* **2019**, *31*, 1.

[21] W. Wang, G. Pedretti, V. Milo, R. Carboni, A. Calderoni, N. Ramaswamy, A. S. Spinelli, D. Ielmini, *Sci. Adv.* **2018**, *4*, 1.

[22] W. Wang, M. Laudato, E. Ambrosi, A. Bricalli, E. Covi, Y. H. Lin, D. Ielmini, *IEEE Trans. Electron Devices* **2019**, *66*, 3802.

[23] C. Qian, J. Sun, L. A. Kong, G. Gou, J. Yang, J. He, Y. Gao, Q. Wan, *ACS Appl. Mater. Interfaces* **2016**, *8*, 26169.

[24] P. Gkoupidenis, N. Schaefer, X. Strakosas, J. A. Fairfield, G. G. Malliaras, *Appl. Phys. Lett.* **2015**, *107*

[25] S. Yu, *Proc. IEEE* **2018**, *106*, 260.

[26] D. S. Jeong, C. S. Hwang, *Adv. Mater.* **2018**, *30*, 1704729.

[27] S. Asapu, N. K. Upadhyay, J. Joshua Yang, Z. Wang, H. Jiang, Q. Xia, *Adv. Mater. Technol.* **2019**, *4*, 1800589.

[28] R. Noriega, J. Rivnay, K. Vandewal, F. P. V. Koch, N. Stingelin, P. Smith, M. F. Toney, A. Salleo, *Nat. Mater.* **2013**, *12*, 1038.

[29] Y. Horii, M. Ikawa, K. Sakaguchi, M. Chikamatsu, Y. Yoshida, R. Azumi, H. Mogi, M. Kitagawa, H. Konishi, K. Yase, *Thin Solid Films* **2009**, *518*, 642.

[30] H. Yang, S. W. Lefevre, C. Y. Ryu, Z. Bao, *Appl. Phys. Lett.* **2007**, *90*, 172116.

[31] D. O. Hebb, *The Organization of Behavior*, Wiley, New York, **1949**.

[32] J. O. Guardado, A. Salleo, *Adv. Funct. Mater.* **2017**, *27*, 1701791.

[33] E. M. Thomas, M. A. Brady, H. Nakayama, B. C. Popere, R. A. Segalman, M. L. Chabinyc, *Adv. Funct. Mater.* **2018**, *28*, 1803687.

[34] R. Giridharagopal, L. Q. Flagg, J. S. Harrison, M. E. Ziffer, J. Onorato, C. K. Luscombe, D. S. Ginger, *Nat. Mater.* **2017**, *16*, 737.

[35] M. J. Panzer, C. D. Frisbie, *J. Am. Chem. Soc.* **2007**, *129*, 6599.

[36] T. Kawai, M. Nakazono, K. Yoshino, *J. Mater. Chem.* **1992**, *2*, 903.

[37] S.-I Kim, Y. Lee, M.-H Park, G.-T. Go, Y.-H. Kim, W. Xu, H.-D. Lee, H. Kim, D.-G. Seo, W. Lee, T.-W. Lee, *Adv. Electron. Mater.* **2019**, *5*, 1900008.

[38] S. Thiemann, S. Sachnov, S. Porscha, P. Wasserscheid, J. Zaumseil, *J. Phys. Chem. C* **2012**, 13536.

[39] A. M. O'Mahony, D. S. Silvester, L. Aldous, C. Hardacre, R. G. Compton, *J. Chem. Eng. Data* **2008**, *53*, 2884.

[40] R. A. John, J. Ko, M. R. Kulkarni, N. Tiwari, N. A. Chien, N. G. Ing, W. L. Leong, N. Mathews, *Small* **2017**, *13*, 15.

[41] V. Milo, G. Pedretti, R. Carboni, A. Calderoni, N. Ramaswamy, S. Ambrogio, D. Ielmini, *Tech. Dig. - Int. Electron Devices Meet. IEDM* **2017**, 16.8.1.

[42] K. Rahimi, I. Botiz, J. O. Agumba, S. Motamen, N. Stingelin, G. Reiter, *RSC Adv.* **2014**, *4*, 11121.

[43] M. Brinkmann, *J. Polym. Sci. Part B Polym. Phys.* **2011**, *49*, 1218.

[44] A. Zen, J. Pflaum, S. Hirschmann, W. Zhuang, F. Jaiser, U. Asawapirom, J. P. Rabe, U. Scherf, D. Neher, *Adv. Funct. Mater.* **2004**, *14*, 757.

[45] R. J. Kline, M. D. McGehee, E. N. Kadnikova, J. Liu, J. M. J. Fréchet, M. F. Toney, *Macromolecules* **2005**, *38*, 3312.

[46] C. Scharsich, R. H. Lohwasser, M. Sommer, U. Asawapirom, U. Scherf, M. Thelakkat, D. Neher, A. Köhler, *J. Polym. Sci. Part B Polym. Phys.* **2012**, *50*, 442.

[47] N. J. Hestand, F. C. Spano, *Chem. Rev.* **2018**, *118*, 7069.

[48] J. Clark, J. F. Chang, F. C. Spano, R. H. Friend, C. Silva, *Appl. Phys. Lett.* **2009**, *94*, 2007.

[49] X. M. Jiang, R. Osterbacka, O. Korovyanko, C. P. An, B. Horovitz, R. A. J. Janssen, Z. V. Vardeny, *Adv. Funct. Mater.* **2002**, *12*, 587.

[50] S. T. Turner, P. Pingel, R. Steyrleuthner, E. J. W. Crossland, S. Ludwigs, D. Neher, *Adv. Funct. Mater.* **2011**, *21*, 4640.

[51] J. Hynynen, D. Kiefer, L. Yu, R. Kroon, R. Munir, A. Amassian, M. Kemerink, C. Müller, *Macromolecules* **2017**, *50*, 8140.

[52] J. Lee, L. G. Kaake, J. H. Cho, X.-Y. Zhu, T. P. Lodge, C. D. Frisbie, *J. Phys. Chem. C* **2009**, *113*, 8972.

[53] C. Enengl, S. Enengl, S. Pluczyk, M. Havlicek, M. Lapkowski, H. Neugebauer, E. Ehrenfreund, *ChemPhysChem* **2016**, *17*, 3830.

[54] C. Y. Gao, M. Pei, H. J. Choi, H. Yang, *Adv. Funct. Mater.* **2019**, *29*, 1903164.

[55] J. F. Chang, B. Sun, D. W. Breiby, M. M. Nielsen, T. I. Sölling, M. Giles, I. McCulloch, H. Sirringhaus, *Chem. Mater.* **2004**, *16*, 4772.

[56] B. J. Thompson, *Opt. Eng.* **1997**, *36*, 1581.

[57] J. H. Cho, J. Lee, Y. He, B. Kim, T. P. Lodge, C. D. Frisbie, *Adv. Mater.* **2008**, *20*, 686.

[58] J. Jang, H. Hwang, C. di Nolfo, E. U. Giacometti, S. Sidler, I. Boybat, B. N. Kurdi, G. W. Burr, R. M. Shelby, P. Narayanan, R. S. Shenoy, K. Virwani, *IEEE Trans. Electron Devices* **2015**, *62*, 3498.

[59] S. T. Keene, A. Melianas, E. J. Fuller, Y. Van De Burgt, A. A. Talin, A. Salleo, *J. Phys. D. Appl. Phys.* **2018**, *51*.

[60] P. Y. Chen, B. Lin, I. T. Wang, T. H. Hou, J. Ye, S. Vrudhula, J. S. Seo, Y. Cao, S. Yu, *2015 IEEE/ACM Int. Conf. Comput. Des. ICCAD 2015*, **2016**, p. 194.

[61] B. Kevin, L. Moshe, *UCI Machine Learning Repository*, University of California at Irvine, School of Information and Computer Science, Irvine, CA **2016**.

[62] Y. LeCun, C. Cortes, C. J. Burges, *The MNIST Database of Handwritten Digits*, National Institute of Standards and Technology, Gaithersburg, MD **2016**.

[63] E. J. Fuller, F. El Gabaly, F. Léonard, S. Agarwal, S. J. Plimpton, R. B. Jacobs-Gedrim, C. D. James, M. J. Marinella, A. A. Talin, *Adv. Mater.* **2017**, *29*, 1604310.

[64] S. Choi, S. H. Tan, Z. Li, Y. Kim, C. Choi, P.-Y. Chen, H. Yeon, S. Yu, J. Kim, *Nat. Mater.* **2018**, *17*, 335.

[65] Y. Ito, A. A. Virkar, S. Mannsfeld, J. H. Oh, M. Toney, J. Locklin, Z. Bao, *J. Am. Chem. Soc.* **2009**, *131*, 9396.